Inorganic Chemistry

Article

pubs.acs.org/IC

Polar and Magnetic Layered A-Site and Rock Salt B-Site-Ordered $NaLnFeWO_6$ (Ln = La, Nd) Perovskites

M. Retuerto,[†] M. R. Li,[†] A. Ignatov,[‡] M. Croft,[‡] K. V. Ramanujachary,[§] S. Chi,[∥] J. P. Hodges,[∥] W. Dachraoui,[⊥] J. Hadermann,[⊥] T. Thao Tran,[#] P. Shiv Halasyamani,[#] C. P. Grams,[▽] J. Hemberger,[▽] and M. Greenblatt*[,†]

[†]Department of Chemistry and Chemical Biology, Rutgers, The State University of New Jersey, 610 Taylor Road, Piscataway, New Jersey 08854, United States

[‡]Department of Physics and Astronomy, Rutgers, The State University of New Jersey, 136 Frelinghuysen Road, Piscataway, New Jersey 08854, United States

[§]Department of Chemistry and Physics, Rowan University, 210 Mullica Hill Road, Glassboro, New Jersey 08028, United States

[∥]Neutron Sciences Directorate, Oak Ridge National Laboratory, Oak Ridge, Tennessee 37831, United States

[⊥]EMAT, University of Antwerp, Groenenborgerlaan 171, 2020 Antwerp, Belgium

[#]Department of Chemistry, University of Houston, 136 Fleming Building, Houston, Texas 77204-5003, United States

[▽]II. Physikalisches Institut, Universität zu Köln, D-50937 Köln, Germany

ABSTRACT: We have expanded the double perovskite family of materials with the unusual combination of layered order in the A sublattice and rock salt order over the B sublattice to compounds $NaLaFeWO_6$ and $NaNdFeWO_6$. The materials have been synthesized and studied by powder X-ray diffraction, neutron diffraction, electron diffraction, magnetic measurements, X-ray absorption spectroscopy, dielectric measurements, and second harmonic generation. At room temperature, the crystal structures of both compounds can be defined in the noncentrosymmetric monoclinic $P2_1$ space group resulting from the combination of ordering both in the A and B sublattices, the distortion of the cell due to tilting of the octahedra, and the displacement of certain cations. The magnetic studies show that both compounds are ordered antiferromagnetically below $T_N \approx 25$ K for $NaLaFeWO_6$ and at ~21 K for $NaNdFeWO_6$. The magnetic structure of $NaNdFeWO_6$ has been solved with a propagation vector $k = (^1/_2\ 0\ ^1/_2)$ as an antiferromagnetic arrangement of Fe and Nd moments. Although the samples are potential multiferroics, the dielectric measurements do not show a ferroelectric response.

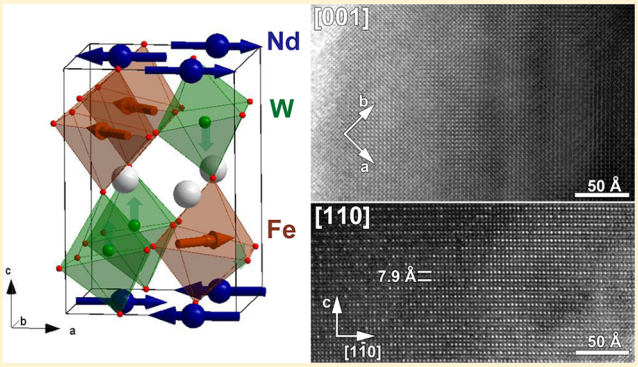

INTRODUCTION

The perovskite-related materials are extensively studied in materials science because of their diverse interesting and useful properties including ferromagnetism, ferroelectricity, multiferroelectricity, superconductivity, and colossal magnetoresistance.[1−5] In the ideal perovskite structure (ABO_3), the BO_6 octahedra share corners to form a 3D framework, and the larger A cations reside in the 12 coordinated cuboctahedral cavities of the framework structure. There are more complex perovskites with two (or more) cations of different valences located in equivalent crystallographic positions, and these cations could be ordered or disordered over these positions. The cation order−disorder plays a critical role in the properties of the perovskites, such as the magnetic ordering, conductivity, and magnetoresistance.[6] The rock salt-type B-site ordering is the most commonly observed, and many examples have been reported. These are the double perovskites $A_2BB'O_6$, where two different cations are ordered or partially ordered over the B position of the structure. Numerous reviews of the B-site-ordered perovskites have been published.[7−9] The B-site-layered cationic ordering is more unusual, and only a few Cu-based perovskites have shown this ordering in R_2CuSnO_6 (R = La, Pr, Nd, Sm), $La_{2-x}Sr_xCuSnO_6$, and La_2CuZrO_6.[10−12] Such unique layered ordering is believed to be driven by a strong first-order Jahn−Teller (FOJT) deformation of the CuO_6 octahedra, which results in four short in-plane Cu−O distances and two long apical ones nearly perpendicular to the (CuO_2) and (SnO_2) planes. $NaNb_{1-x}Ta_xO_3$ surprisingly presents short-range B-site-layered ordering, and it is suggested to be due to the difference in effective electronegativity between Nb^{5+} and Ta^{5+}.[13]

Received: June 12, 2013
Published: October 18, 2013

We are interested in compounds with A-site-layered and B-site rock salt ordering. Compared to numerous double perovskites with order in the B sublattice, only some examples have been reported for both A and B cationic ordering ($AA'BB'O_6$). The reason for the uncommon A-site ordering compared to B-site ordering is that the charge difference between A-site cations cannot be as large as it can be for B-site cations and is also due to the inability of any type of A-site ordering to create a stable bonding environment for all anions. In fact, A-site layering and B-site rock salt orderings are synergistic, and the removal of one leads to the disappearance of the other. Some of the double perovskites that present both ordering are $NaLnMWO_6$ and $KLnMWO_6$ (Ln = rare earths; M = Mn, Co, Ni, Mg), $NaLaMgTeO_6$ and $NaLaScNbO_6$.[14−16] A-site-layered ordering seems to be stabilized by the presence of a highly charged d^0 cation with a second-order Jahn−Teller (SOJT) effect on one of the B sites and is also associated with B-site rock salt-type ordering. Some of these phases, $NaLaMnWO_6$, $NaNdMnWO_6$, and $NaTbMnWO_6$, adopt a noncentrosymmetric structure in $P2_1$ symmetry arising from the combination of the cation orderings and $a^-a^-c^+$ octahedral tilting.[14] Thus, the presence of both SOJT distorted d^0 cations and magnetic ions in such compounds potentially could lead to multiferroic behavior.[17] To search for new multiferroic materials, we have prepared the oxides $NaLaFeWO_6$ and $NaNdFeWO_6$ because, according to the known examples, Na^+ and Ln^{3+} are a good combination for achieving A-site-layered ordering, W^{6+} is a SOJT, Fe^{2+} is a magnetic cation, and also the charge difference between Fe^{2+} and W^{6+} is large enough to produce the required B-site ordering.

EXPERIMENTAL SECTION

The oxides were prepared in polycrystalline form by a soft-chemistry procedure designed to obtain reactive precursors. Stoichiometric amounts of Na_2CO_3, La_2O_3 (previously heated to 1000 °C) or Nd_2O_3 (previously heated to 600 °C), $FeC_2O_4{\cdot}2H_2O$, and $(NH_4)_{10}W_{12}O_{41}{\cdot}5H_2O$ were dissolved in an aqueous citric acid solution (10 g of citric acid in 100 mL of water) containing 5 mL of nitric acid. The solution was slowly evaporated, leading to organic resins containing a homogeneous distribution of the involved cations. The resins were dried at 120 °C and decomposed at 600 °C/12 h in air to eliminate the organic materials and nitrates and create homogeneous precursors. Then, for $NaLaFeWO_6$, the precursors were heated at 900 °C/6 h in a H_2/Ar (1%/99%) reducing flow, and for $NaNdFeWO_6$, the precursors were held at 850 °C/2 h in a H_2/N_2 (5%/95%) reducing flow.

The samples were characterized by powder X-ray diffraction (PXD) (Cu Kα_1, λ = 1.5406 Å). For the crystallographic structural refinement, powder neutron diffraction (PND) data were collected at room temperature and 12 K via the POWGEN instrument at the Spallation Neutron Source and for the magnetic structure refinement of $NaNdFeWO_6$ at low temperature (4 K) via the WAND instrument in the High Flux Isotope Reactor, both at Oak Ridge National Laboratory. The patterns were refined by the Rietveld method,[18] with the Fullprof refinement program.[19] Samples for transmission electron microscopy (TEM) were prepared by dispersing the powder in ethanol and depositing it on a holey carbon grid. Selected area electron diffraction (SAED) patterns were obtained on a Philips CM20 transmission electron microscope. High-resolution transmission electron microscopy (HRTEM) was obtained with a Tecnai G2 transmission electron microscope. The composition of the samples was determined with energy-dispersive X-ray (EDX) analysis performed with a JEOL JSM5510 scanning electron microscope on 50 crystallites for each sample, and for each crystal investigated by electron diffraction, EDX was also obtained via the Philips CM20; both instruments were equipped with the Oxford INCA system.

Powder second harmonic generation (SHG) measurements were performed on a modified Kurtz nonlinear optical (NLO) system with a pulsed Nd:YAG laser with a wavelength of 1064 nm. A detailed description of the equipment and methodology has been published.[20] Because the powder SHG efficiency has been shown to depend strongly on the particle size,[21] $NaLaFeWO_6$ was ground and sieved into distinct particle size ranges (<20, 20−45, 45−63, 63−75, 75−90, >90 μm). Attributable to a limited amount of $NaNdFeWO_6$ powder, SHG measurements were performed on ungraded powder. Relevant comparisons with known SHG materials were made by grinding and sieving crystalline α-SiO_2 and $LiNbO_3$ into the same particle size ranges. No index-matching fluid was used in any of the experiments.

The magnetic measurements were performed with a SQUID magnetometer. The dc magnetic susceptibility data were collected from 5 to 400 K under an applied magnetic field of 1000 Oe. Isothermal magnetization curves were obtained in magnetic fields from 5 to −5 T at T = 5 K. X-ray absorption near-edge spectroscopy (XANES) was collected simultaneously in both transmission and fluorescence modes on beamline X-19A at the Brookhaven National Synchrotron Light Source. For the dielectric investigations, electrodes of silver paint were prepared on both sides of sintered pellets with typical dimensions of 0.5 mm thickness and 10 mm^2 area. The spectroscopic permittivity measurements have been performed by employing a frequency response analyzer (Novocontrol) for the frequency range of 1 Hz < ν < 1 MHz with an electric field stimulus of typically 1 V/mm. The $P(E)$ cycling was recorded with an electrometer with an integrated voltage source (Keithley) at an effective frequency of about 50 mHz. The PUND measurements were conducted with an arbitrary function generator (Agilent) together with a high-voltage amplifier.

RESULTS AND DISCUSSION

The samples were obtained as brown, well-crystallized pure powders. EDX analysis indicates chemical compositions of $Na_{0.99(8)}La_{1.01(4)}Fe_{0.91(3)}W_{1.07(9)}O_x$ and $Na_{0.98(5)}Nd_{0.97(14)}Fe_{1.06(16)}W_{0.94(5)}O_x$; thus the compounds are stoichiometric within the standard deviation range of error.

Crystallographic Structure. The PXD patterns are characteristic of a perovskite-type structure (Figure 1). The relatively intense superstructure peaks evidence long-range Na/Ln ordering over the A sites and Fe/W ordering over the B sites. The layered A-site ordering is revealed by the intensity of (0 0 $^1/_2$) and (1 0 $^1/_2$) reflections, and the rock salt B-site ordering is revealed by the intensity of the pseudocubic ($^1/_2$ $^1/_2$ $^1/_2$) reflection. We evaluate that the degree of ordering is complete over both A and B sublattices. Using the PXD data, we could refine the structure of both oxides in different space groups. The most symmetric space group that fits all of the reflections is the tetragonal $P4/nmm$ that accounts for a double perovskite with order in both sublattices but does not allow any rotation of the octahedra. We carried out PND to solve the structure properly. At room temperature, some of the observed reflections could not be indexed in $P4/nmm$. Therefore, the crystal symmetry was lowered to the possible structures generated by octahedral tilting distortions together with A-layered and B-rock salt ordering. A schematic diagram of the possible space groups was reported by Woodward et al.,[16] and there are 12 possible combinations. Following previous studies of similar compounds (e.g., $NaLaMgWO_6$),[22] we analyzed the PND data with the $P2_1/m$ space group, obtained via the out-of-phase octahedral tilting along the [110] direction described as $a^-a^-c^0$ with Glazer notation.[23] However, $P2_1/m$ is not completely consistent with all of the intensities observed. Therefore, the other possible space groups were tried, and monoclinic $P2_1$ (Glazer tilt notation $a^-a^-c^+$) best fit the PND data. Note that $P2_1/m$ and $P2_1$ have the same reflection

dx.doi.org/10.1021/ic401491y | Inorg. Chem. 2013, 52, 12482−12491

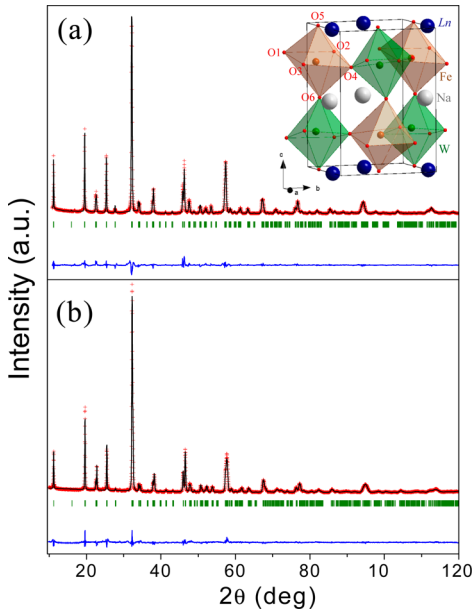

Figure 1. Comparison of the observed (crosses), calculated (solid line,) and difference (bottom) PXD patterns of (a) $NaLaFeWO_6$ and (b) $NaNdFeWO_6$, refined in the $P2_1$ space group. (a, inset) View of the crystal structure: light-gray circles represent Na^+ cations; blue ones, Ln^{3+}; brown ones, Fe^{2+}; green ones, W^{6+}; and red ones, oxygen.

conditions and that they can be distinguished only by differences in the peak intensities. The monoclinic $P2_1$ space group has been previously observed in similar compounds.[14]

In $P2_1$, the unit-cell parameters are related to a_0 (ideal cubic perovskite, $a_0 \approx 3.8$ Å) as $a \approx b \approx 2^{1/2}a_0$, $c \approx 2a_0$. All of the atoms are in $2a$ (x, y, z) general position. There are two crystallographicaly independent positions for Na and La, two for Fe and W, and six nonequivalent oxygen atoms. Figure 2 illustrates the Rietveld refinement of $NaLaFeWO_6$ and $NaNdFeWO_6$ with PND data at room temperature. Tables 1 and 2 summarize the unit-cell, atomic, thermal parameters, and

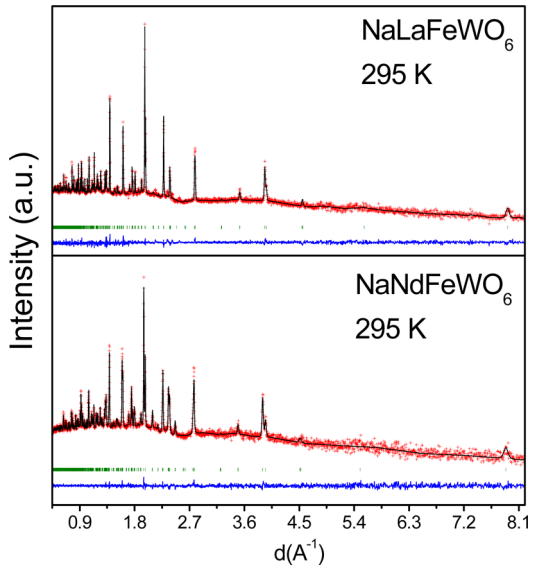

Figure 2. Comparison of the observed (crosses), calculated (solid line), and difference (bottom) PND patterns for $NaLaFeWO_6$ and $NaNdFeWO_6$ at $T = 295$ K.

discrepancy factors. Table 3 contains the main interatomic distances and angles. A schematic view of the structure is shown in the inset of Figure 1. Tables 4 and 5 show the crystallographic parameters after the refinement of the structure at low temperature (12 K) in the same space group, and in Table 3 the bond distances, angles, and bond valence sums of both samples at low temperature are given. It should be highlighted that the octahedral tilting together with the displacement of some cations (see below) breaks the inversion center, generating a noncentrosymmetric structure, and because there are magnetic cations, multiferroic behavior could be expected. A tilt series of electron diffraction (ED) patterns were collected for $NaLaFeWO_6$. The patterns in Figure 3 could be indexed in the unit cell derived from PND. The reflection conditions derived from the ED patterns are only $0k0$: $k = 2n$, in agreement with the $P2_1$ space group. The $0k0$: $k = 2n + 1$ reflections are present on the [100] pattern because of double diffraction, and their systematic extinction was verified by their disappearance during the tilt around this axis. The [001] pattern also contains reflections at positions $^1/_2(oo0)$ (o = odd index), but these are due to twinning with the [110] pattern in two 90°-rotated variants (because these zones are equivalent in the parent perovskite cell) and are not part of the [001] pattern itself. The very weak reflections in the [110] pattern itself have the same origin a 90°-rotation twin. In addition to these reflections that correspond to those found in the PND data, there is a set of weak satellite reflections with modulation vector $q \approx {}^1/_{12}a^* + {}^1/_{12}b^*$, as we will discuss below.

The refinement of the crystal structures confirms the displacement of W^{6+} cations from the center of the octahedra closer to the layers with the monovalent Na^+ cations. This displacement occurs because of the SOJT distortion of the W^{6+} cation, which moves to achieve the stability necessary for these phases to be formed.[16] Tungsten displacement is well known in other compounds (e.g., WO_3,[24,25]) and is favored when the energy gap is small between empty W 5d and filled O 2p orbitals. We confirm the displacement of W by comparing the W−O distances along c. In both compounds, W−O5 (oxygen in rare earth planes) is quantitatively longer than W−O6 (oxygen in Na planes). For the La sample, W−O5 = 2.088(3) Å whereas W−O6 = 1.876(3) Å, and for Nd, W−O5 = 2.089(3) Å and W−O6 = 1.865(3) Å (Table 3). This displacement may be compared to the FeO_6 octahedra, which remain mostly symmetric, and all of the the Fe−O distances are ∼2 Å. The monoclinic structure arises from the antiphase rotation of the octahedra with respect to both a and b axes and the in-phase rotation with respect to the c axis, so all Fe−O−W bond angles are different and smaller than 180°. The angles become smaller from the La to the Nd compound, indicating a higher degree of octahedra tilting in $NaNdFeWO_6$ as a result of the smaller size of Nd^{3+} compared to that of La^{3+}. This also shows up in the unit-cell parameters that are smaller in $NaNdFeWO_6$ (V = 240.09(2) Å^3) than in $NaLaFeWO_6$ (V = 244.86(3) Å^3). The calculation of the bond-valence sums[26] allowed an estimation of the oxidation states of the ions (Table 3), being closer to Fe^{2+} and W^{6+} than to Fe^{3+} and W^{5+}, and all of the oxygen ions are close to 2, indicating a proper environment for oxygen in the structure.

Figure 4 shows HRTEM images of $NaLaFeWO_6$ along the [001] and [110] directions. On the image taken along [001], alternating bright and dark bands are present perpendicular to the [110] = a_0 direction, with an average periodicity of $12a_0$ corresponding to the modulation with modulation vector $q \approx$

dx.doi.org/10.1021/ic401491y | Inorg. Chem. 2013, 52, 12482−12491

Table 1. Structural Parameters after the Refinement of the Crystal Structure of $NaLaFeWO_6$ from PND Data at 295 K[a]

atom	position	x	y	z	B(Å^2)	occupancy
Na	2a	0.2792(6)	0.4830(8)	0.5023(4)	0.19(1)	1.0
La	2a	0.2532(3)	0.50373(7)	0.0008(3)	0.19(1)	1.0
Fe	2a	0.2487(2)	0.0050(5)	0.7452(2)	0.112(6)	1.0
W	2a	0.2521(4)	0.0003(6)	0.2607(2)	0.112(6)	1.0
O1	2a	0.0282(5)	0.2690(7)	0.2011(3)	1.125(9)	1.0
O2	2a	0.0039(6)	0.2799(6)	0.7936(3)	1.125(9)	1.0
O3	2a	0.4706(5)	0.2792(6)	0.2514(3)	1.125(9)	1.0
O4	2a	0.4901(6)	0.2927(7)	0.7138(2)	1.125(9)	1.0
O5	2a	0.3170(3)	0.0069(7)	0.0011(3)	1.125(9)	1.0
O6	2a	0.2154(4)	0.0539(5)	0.4932(3)	1.125(9)	1.0

[a]Space group $P2_1$, $Z = 4$. Unit-cell parameters: $a = 5.5616(4)$ Å, $b = 5.5617(4)$ Å, $c = 7.9163(3)$ Å, $\beta = 90.177(5)°$, $V = 244.86(3)$ Å^3. Discrepancy factors: (pattern 1) $R_p = 1.98\%$, $R_{wp} = 2.40\%$, $R_{exp} = 0.96\%$, $R_{Bragg} = 6.88\%$, and $\chi^2 = 6.19$; (pattern 2) $R_p = 4.07\%$, $R_{wp} = 4.16\%$, $R_{exp} = 2.71\%$, $R_{Bragg} = 8.12\%$, and $\chi^2 = 2.36$.

Table 2. Structural Parameters after the Refinement of the Crystal Structure of $NaNdFeWO_6$ from PND Data at 295 K[a]

atom	position	x	y	z	B(Å^2)	occupancy
Na	2a	0.2640(3)	0.5151(4)	0.5194(2)	0.36(9)	1.0
Nd	2a	0.2413(2)	0.5540(3)	0.0031(2)	0.36(9)	1.0
Fe	2a	0.2469(2)	0.0070(4)	0.7445(1)	0.39(7)	1.0
W	2a	0.2570(4)	0.02102(4)	0.2651(2)	0.39(7)	1.0
O1	2a	0.0440(3)	0.2790(4)	0.1981(2)	1.10(6)	1.0
O2	2a	0.0141(3)	0.2870(4)	0.8080(2)	1.10(6)	1.0
O3	2a	0.5420(3)	0.1980(3)	0.2730(2)	1.10(6)	1.0
O4	2a	0.4490(3)	0.7301(4)	0.2800(2)	1.10(6)	1.0
O5	2a	0.3300(3)	0.0001(4)	0.0060(3)	1.10(6)	1.0
O6	2a	0.1700(2)	0.0360(4)	0.4930(3)	1.10(6)	1.0

[a]Space group $P2_1$, $Z = 4$. Unit-cell parameters: $a = 5.5016(3)$ Å, $b = 5.5293(3)$ Å, $c = 7.8927(3)$ Å, $\beta = 90.183(6)°$, $V = 240.09(2)$ Å^3. Discrepancy factors: (pattern 1) $R_p = 2.16\%$, $R_{wp} = 1.99\%$, $R_{exp} = 1.28\%$, $R_{Bragg} = 7.46\%$, and $\chi^2 = 2.42$; (pattern 2) $R_p = 4.49\%$, $R_{wp} = 4.10\%$, $R_{exp} = 3.11\%$, $R_{Bragg} = 8.51\%$, and $\chi^2 = 1.74$.

$^1/_{12}a^* + {}^1/_{12}b^*$ found for Figure 3. The image taken along [110] shows clearly the doubling of the c parameter compared to the parent perovskite structure as a result of the layering of the A cations. This periodic nanoscale phase separation is very unusual, and it has been observed in Li-containing perovskite phases such as $(Nd_{2/3-x}Li_{3x}O_3)TiO_3$.[27] The superlattice in this case consists of domains of $NdLiTi_2O_6$ separated by Li-free regions of $Nd_{4/3}Ti_2O_6$. This kind of periodic phase separation has also been observed in related $NaLnMgWO_6$ and $NaLnMnWO_6$ phases.[28−30] For $NaLaMgWO_6$, the modulation occurs in one dimension, leading to a striped pattern of light and dark regions very similar to our case; a compositional analysis indicated separation into Na-rich ($NaLaMgWO_6$) and Na-deficient ($La_{4/3}MgWO_6$) phases. It appears that the A-site cationic ordering induces instabilities, producing complex structural and compositional modulations.

Second Harmonic Generation Results. Because $NaLaFeWO_6$ and $NaNdFeWO_6$ crystallize in the noncentrosymmetric $P2_1$ space group, we investigated their SHG properties. The SHG response, using 1064 nm radiation on ungraded powder, shows that $NaNdFeWO_6$ has an SHG intensity roughly equal to that of α-SiO_2. Powder SHG measurements on $NaLaFeWO_6$ also revealed an SHG efficiency approximately equal to that of α-SiO_2 in the 45−63 μm particle size range. Additional SHG measurements, providing the particle size versus SHG efficiency, indicate that $NaLaFeWO_6$ exhibits type 1 phase-matching behavior. As such, $NaLaFeWO_6$ falls into the class B category of SHG materials, as defined by Kurtz and Perry (Figure 5).[31] On the basis of these measurements, we estimate an average NLO susceptibility of $NaLaFeWO_6$, $\langle d_{eff}\rangle_{exp}$, of approximately 1.2 pm/V. By these results, we confirm the noncentrosymmetric character of the structure of both $NaLaFeWO_6$ and $NaNdFeWO_6$ phases.

XANES Results. XANES of Fe and W in $NaLaFeWO_6$ was used to determine the oxidation states. The L_3 edge of 5d-row compounds is dominated by an intense "white line" (WL) feature involving transitions into empty d final states. For octahedrally coordinated perovskites such as Sr_2MnWO_6, Sr_2MnReO_6, and $NaLaFeWO_6$ (Figure 6a), the WL features are distinctly bimodal with unresolved A and B features associated with transitions into the empty 6-fold-degenerate t_{2g} and 4-fold-degenerate e_g final 5d states.[32−34] The A−B feature splitting reflects the ligand-field splitting of the 5d orbitals, and their relative intensities can indicate the nominal 5d orbital hole (electron) count. Specifically, the A-feature peak intensity goes from being larger than the B feature in an ~$5d^0$ compound (see Sr_2MnWO_6 in Figure 6a) to being smaller in an ~$5d^1$ compound (see Sr_2MnReO_6 in the upper inset of Figure 6a), where one t_{2g} hole state has been filled. The A−B feature structure of $NaLaFeWO_6$ indicates an ~W^{6+} d^0 configuration. However, the A−B splitting in $NaLaFeWO_6$ is reduced to 2.7 eV from 3.9 eV in Sr_2MnWO_6, indicating a smaller ligand-field splitting in the former, and the centrum of the WL feature is shifted to somewhat lower energy relative to that of Sr_2MnWO_6, indicating the presence of some W^{5+}. Figure 6b shows the Fe−K main edge spectra for the following standards that have corner-sharing Fe−O octahedra: Fe^{2+}, $LiFePO_4$; Fe^{3+}, La_2VFeO_6; and ~Fe^{4+}, $SrFeO_{3-\delta}$.[35,36] Studies of K edges of 3d

dx.doi.org/10.1021/ic401491y | Inorg. Chem. 2013, 52, 12482−12491

Table 3. Main Interatomic Distances (Angstroms) and Angles (Degrees) for $NaLnFeWO_6$ (Ln = La, Nd) at 295 and 12 K

	$NaLaFeWO_6$		$NaNdFeWO_6$	
	295 K	12 K	295 K	12 K
	Bond Distances			
Fe−O(1)	2.069(4)	2.063(13)	2.088(2)	2.104(9)
Fe−O(2)	2.084(4)	2.123(12)	2.072(3)	2.097(9)
Fe−O(3)	2.004(4)	1.988(13)	2.071(3)	2.035(8)
Fe−O(4)	2.104(4)	2.078(13)	2.088(2)	2.096(8)
Fe−O(5)	2.060(3)	2.059(11)	2.113(3)	2.100(8)
Fe−O(6)	2.021(3)	2.013(13)	2.035(2)	2.070(7)
Fe−O average	2.057	2.054	2.078	2.084
W−O(1)	2.001(4)	1.99(2)	1.919(2)	1.92(1)
W−O(2)	1.926(4)	1.95(2)	2.056(3)	2.02(1)
W−O(3)	1.972(4)	1.96(2)	1.849(2)	1.88(1)
W−O(4)	1.851(4)	1.85(2)	1.928(2)	1.925(9)
W−O(5)	2.088(3)	2.08(1)	2.089(3)	2.112(9)
W−O(6)	1.876(3)	1.90(1)	1.865(3)	1.819(8)
W−O average	1.952	1.953	1.951	1.946
	Bond Valence Sums			
Ln	2.961(9)	2.98(3)	2.811(6)	2.811(6)
Na	0.745(5)	0.777(9)	0.886(3)	0.886(3)
Fe	2.52(1)	2.54(3)	2.375(7)	2.375(7)
W	5.8(3)	5.54(1)	5.63(2)	5.63(2)
O1	1.99(1)	2.07(4)	2.100(8)	2.100(8)
O2	2.07(1)	2.13(5)	1.885(6)	1.885(6)
O3	1.89(1)	1.87(5)	2.201(9)	2.201(9)
O4	2.05(2)	2.01(5)	1.838(7)	1.838(7)
O5	1.962(7)	1.97(3)	1.796(6)	1.796(6)
O6	1.84(1)	1.79(5)	1.886(9)	1.886(9)
	Bond Angles			
Fe−O(1)−W	152.7(3)	154(1)	148.9(2)	146.4(6)
Fe−O(2)−W	155.3(3)	154(1)	148.3(2)	148.8(6)
Fe−O(3)−W	166.6(3)	158(1)	155.5(2)	155.5(6)
Fe−O(4)−W	162.9(3)	164(1)	157.9(2)	156.8(6)
Fe−O(5)−W	159.4(2)	158.3(8)	156.0(1)	154.6(4)
Fe−O(6)−W	159.5(2)	160.1(9)	152.2(2)	152.3(5)

transition metals in oxides (with corner-sharing octahedral coordination) typically show a chemical shift in the energy of the main edge peak (see P_{2+}, P_{3+}, and P_{4+} in Figure 6b) upon increasing the metal valence.[37] The Fe^{2+} (FeO) standard has been included; it has octahedral coordination but with edge-sharing octahedra. The P_{2+} peak of the corner-sharing compounds lies between a shoulder feature (shifted down in energy) and the absolute peak (shifted up in energy) of the edge-sharing FeO spectrum, as has been seen in Mn-based compounds.[38] The Fe−K edge of $NaLaFeWO_6$ manifests a clear, sharp peak at an energy P_{2+} characteristic of an Fe^{2+} compound.

Magnetic Measurements. The dc susceptibility versus temperature for $NaLaFeWO_6$ and $NaNdFeWO_6$, displayed in Figure 7a, shows similar behavior for both compounds. There is an antiferromagnetic (AFM) transition at ∼25 K for $NaLaFeWO_6$ and at ∼21 K for $NaNdFeWO_6$, with a subsequent and progressive reduction of the magnetization when the temperature rises. For $NaNdFeWO_6$, below the magnetic transition temperature, an increment in the susceptibility occurs that is attributed to the polarization of the Nd magnetic moments that couple with the Fe^{2+} moments. This is not observed in $NaLaFeWO_6$ because La cations are not magnetic. The low transition temperature of both materials could be attributed to the localization of the magnetic ions in the unit cell. As shown by XANES, the compounds present Fe^{2+} and W^{6+}, thus the only magnetic cation with a possible magnetic order at high temperature is Fe^{2+} because Nd orders at low temperatures. Fe and W are crystallographically completely ordered, so the magnetic paths are along the superexchange interactions Fe−O−W−O−Fe. Hence the indirect interaction between Fe spins would result in low magnetic ordering temperatures together with the nonlinearity of these interactions because the Fe/W octahedra are highly tilted. Furthermore, the magnetic transition temperature looks lower in the Nd than in the La compound, possibly because of the smaller effective size of Nd^{3+} relative to La^{3+}, which produce more bending of the Fe−O−W bond angles in Nd (Table 3), reducing the linearity of the Fe−O−W−O−Fe magnetic paths (or orbital overlap) and thereby decreasing the strength of the magnetic interactions and the magnetic transition temperature in $NaNdFeWO_6$.

Zero-field-cooled (ZFC) and field-cooled (FC) curves in both cases overlap at high temperatures but diverge on decreasing the temperature below 150−200 K, indicating the presence of magnetic frustration in both systems. The magnetic properties are very similar to those found in the $NaLnMnWO_6$ series, which have also been reported to be AFMs.[39] In our samples, above the magnetic transition temperature the compounds do not follow the linear behavior characteristic of the Curie−Weiss law, and the noticeable deviation could

Table 4. Structural Parameters after the Refinement of the Crystal Structure of $NaLaFeWO_6$ from PND Data at 12 K[a]

atom	position	x	y	z	B(Å^2)	occupancy
Na	2a	0.266(2)	0.511(2)	0.504(2)	0.29(4)	1.0
La	2a	0.2414(9)	0.5084(9)	0.001(1)	0.28(1)	1.0
Fe	2a	0.2504(9)	0.023(2)	0.7452(7)	0.06(2)	1.0
W	2a	0.258(2)	0.025(1)	0.258(1)	0.06(2)	1.0
O1	2a	0.002(2)	0.262(2)	0.201(1)	0.63(2)	1.0
O2	2a	0.0001(2)	0.302(2)	0.799(2)	0.63(2)	1.0
O3	2a	0.468(2)	0.307(2)	0.288(1)	0.63(2)	1.0
O4	2a	0.479(2)	0.319(2)	0.732(1)	0.63(2)	1.0
O5	2a	0.3244(1)	0.023(2)	0.001(1)	0.63(2)	1.0
O6	2a	0.226(1)	0.078(1)	0.494(1)	0.63(2)	1.0

[a]Space group $P2_1$, Z = 4. Unit-cell parameters: a = 5.5515(5) Å, b = 5.5505(4) Å, c = 7.9028(3) Å, β = 90.184(5)°, V = 243.51(3) Å^3. Discrepancy factors: (pattern 1) R_p = 2.56%, R_{wp} = 3.07%, R_{exp} = 0.98%, R_{Bragg} = 7.05%, and χ^2 = 9.7; (pattern 2) R_p = 4.04%, R_{wp} = 4.75%, R_{exp} = 2.22%, R_{Bragg} = 5.41%, and χ^2 = 4.58.

dx.doi.org/10.1021/ic401491y | Inorg. Chem. 2013, 52, 12482−12491

Table 5. Structural Parameters after the Refinement of the Crystal Structure of $NaNdFeWO_6$ from PND Data at 12 K[a]

atom	position	x	y	z	B(Å^2)	occupancy
Na	2a	0.261(1)	0.5111(9)	0.5172(6)	0.20(2)	1.0
Nd	2a	0.2443(6)	0.5520(3)	0.0026(6)	0.20(2)	1.0
Fe	2a	0.249(1)	0.0036(6)	0.7445(4)	0.17(1)	1.0
W	2a	0.254(2)	0.0181(9)	0.2656(6)	0.17(1	1.0
O1	2a	0.047(1)	0.278(1)	0.1939(9)	0.73(2)	1.0
O2	2a	0.020(1)	0.296(1)	0.8034(8)	0.73(2)	1.0
O3	2a	0.543(1)	0.200(1)	0.2771(9)	0.73(2)	1.0
O4	2a	0.444(1)	0.725(1)	0.2813(8)	0.73(2)	1.0
O5	2a	0.3354(9)	0.003(1)	0.0041(9)	0.73(2)	1.0
O6	2a	0.1716(9)	0.038(1)	0.4883(8)	0.73(2)	1.0

[a]Space group $P2_1$, Z = 4. Unit-cell parameters: a = 5.4938(2) Å, b = 5.5137(2) Å, c = 7.8836(3) Å, β = 90.199(5)°, V = 238.80(2) Å^3. Discrepancy factors: (pattern 1) R_p = 2.20%, R_{wp} = 2.11%, R_{exp} = 0.91%, R_{Bragg} = 3.33%, and χ^2 = 5.39; (pattern 2) R_p = 4.10%, R_{wp} = 4.80%, R_{exp} = 2.00%, R_{Bragg} = 11.9%, and χ^2 = 5.77.

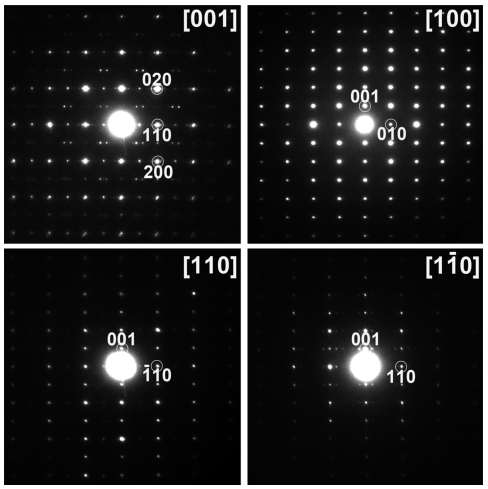

Figure 3. SAED of $NaLaFeWO_6$ indexed in the parent perovskite cell.

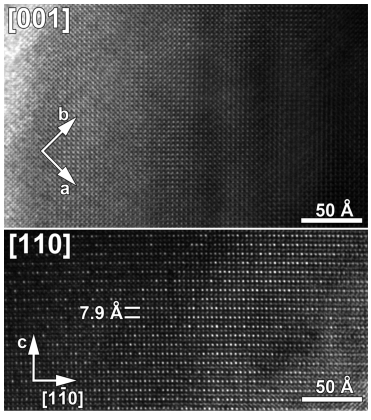

Figure 4. HRTEM images of $NaLaFeWO_6$ along the [001] and [110] directions.

indicate that there are magnetic correlations at high temperature or magnetic impurities, removing the possibility to calculate the Curie−Weiss parameters. The isothermal magnetization curves measured at 5 K are displayed in Figure 7b. Both samples present a small curvature indicating that they are not perfect AFMs. This curvature points out the magnetic complexity in the compounds and may be attributed to the formation of a glassy magnetic state or magnetic impurities, as is also indicated by the ZFC-FC divergence.

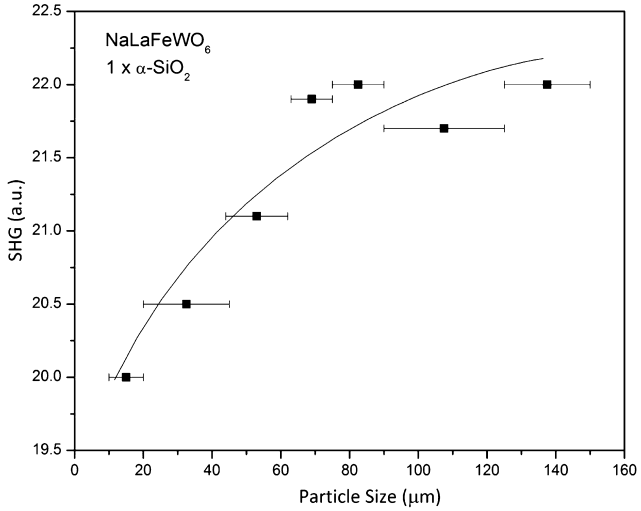

Figure 5. Powder second harmonic generation for $NaLaFeWO_6$.

Magnetic Structure. The eventual establishment of a magnetic ordered phase was followed from sequential PND data in the temperature interval of T = 4−300 K for $NaNdFeWO_6$. For $NaLaFeWO_6$ (Figure 8a), the low-temperature PND, measured in POWGEN at 12 K, does not show any magnetic contributions to the low-angle reflections, which would be ascribed to the establishment of long-range magnetic ordering between Fe spins. However, the magnetic properties show the establishment of a magnetic transition at around 25 K but with a net magnetic moment of ∼0.5μ_B/mol, which suggests that the value is not large enough to be detectable by PND techniques because the only magnetically ordered atom is Fe^{2+}, and Fe^{2+} atoms are not consecutive but are separated by W^{6+} octahedra, or because the magnetic contribution is observed only below 12 K, although the magnetic transition occurs at around 25 K.

For $NaNdFeWO_6$, new magnetic diffraction peaks are observed at temperatures below 25 K (Figure 8b). These new peaks are forbidden for the crystallographic Bragg reflections in space group $P2_1$. The peaks correspond to magnetic satellites defined by the propagation vector k = ($^1/_2$, 0, $^1/_2$). There are two magnetic species: Fe and Nd. The two magnetic Fe atoms of the unit cell, Fe1 at (x, y, z) and Fe2 at ($-x$, y + $^1/_2$, $-z$), are magnetically coupled as $-m_{1x} = m_{2x} = 1.8(3)\mu_B$, $m_{1y} = m_{2y} = 2.2(2)\mu_B$, and $m_{1z} = m_{2z} = 0$. And both Nd moments, Nd1 at (x, y, z) and Nd2 at ($-x$, y + $^1/_2$, $-z$) are

dx.doi.org/10.1021/ic401491y | Inorg. Chem. 2013, 52, 12482−12491

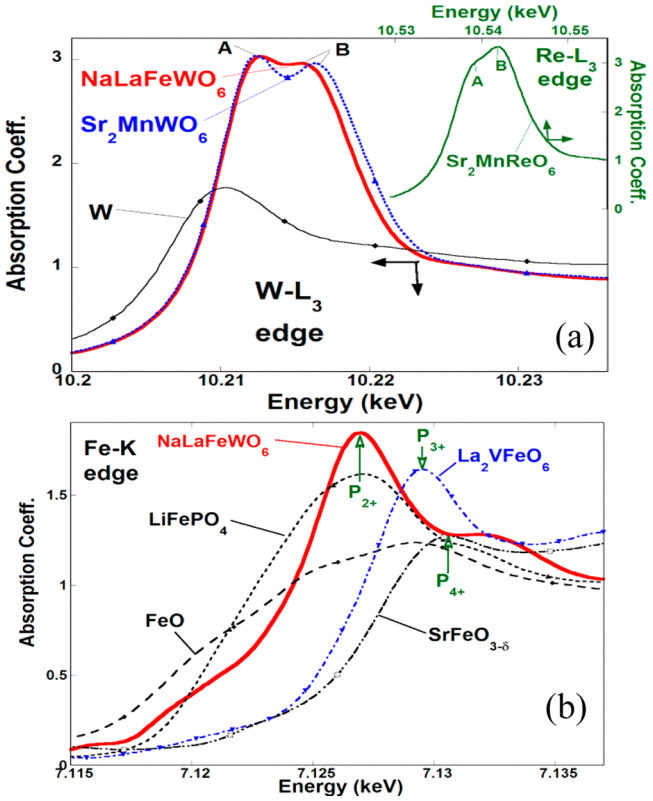

Figure 6. (a) W-L_3 edges of $NaLaFeWO_6$ and ~d^0-W^{6+} standard Sr_2MnWO_6. (Inset) For comparison, the Re-L_3 edge of ~d^1-Re^{6+} standard Sr_2MnReO_6. (b) Fe-K edges of $NaLaFeWO_6$ along with several standards.

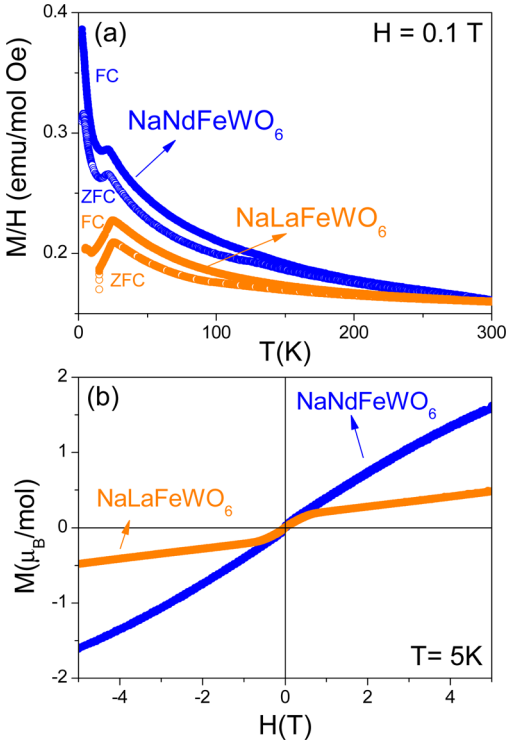

Figure 7. (a) Thermal evolution of the field-cooling (FC) and zero-field-cooling (ZFC) dc susceptibility of $NaLaFeWO_6$ and $NaNdFeWO_6$. (b) Magnetization vs magnetic field isotherms for $NaLaFeWO_6$ and $NaNdFeWO_6$.

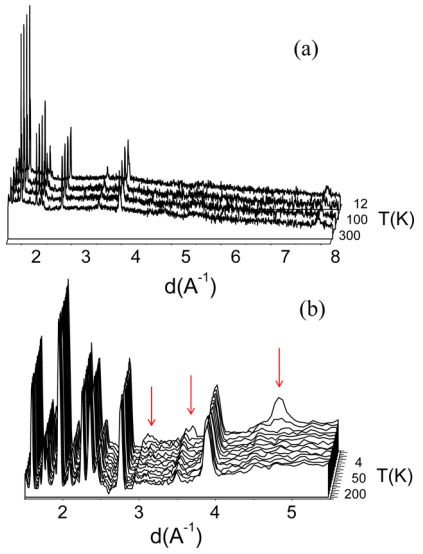

Figure 8. Thermal evolution of the PND patterns for (a) $NaLaFeWO_6$ and (b) $NaNdFeWO_6$.

ordered only on the x axis as $m_{1x} = m_{2x} = 2.7(4)\mu_B$. Figure 9a shows the final Rietveld plot including the crystallographic and

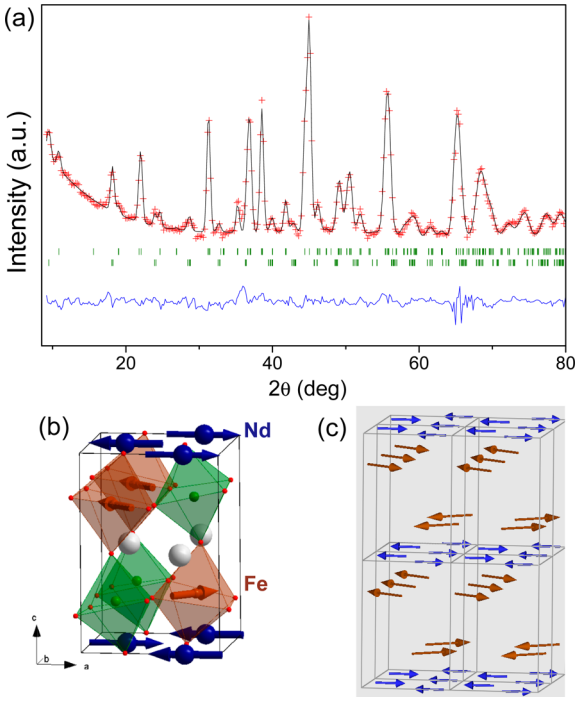

Figure 9. (a) Rietveld fit at 4 K from PND data for $NaNdFeWO_6$. Observed (circles), calculated (solid line), and difference (bottom) profiles. Both Bragg lines correspond to the crystallographic and magnetic structures. (b) Unit-cell and (c) eight-unit-cell representation of the magnetic structure of $NaNdFeWO_6$ with the magnetic moments plotted on the Fe and Nd atoms; the crystal structure is monoclinic, and the propagation vector is $k = (^1/_2, 0, ^1/_2)$.

magnetic phases. The collinear magnetic structure is shown in Figure 9b,c. It can be described as ferromagnetic columns of Fe and Nd moments along the b direction that are coupled antiferromagnetically. Nd moments are ordered as a stacking of $(++--++--)$ magnetic interactions along the a axis. This

dx.doi.org/10.1021/ic401491y | Inorg. Chem. 2013, 52, 12482−12491

configuration has been previously observed in oxides such as $NdNiO_3$.[40]

Dielectric Characterization. To investigate the dielectric properties and possible magnetoelectric coupling effects near the magnetic transitions, we conducted measurements of the complex dielectric permittivity. Figure 10 shows the results for

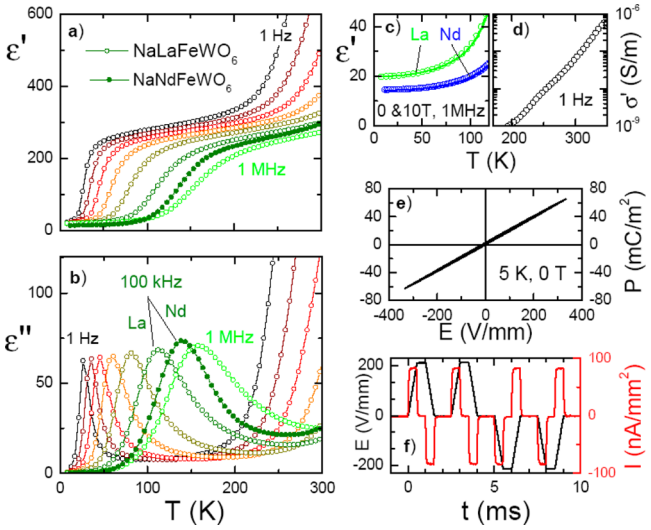

Figure 10. (a, b) Temperature dependence of the real and imaginary parts of the dielectric permittivity of $NaLaFeWO_6$ (○) measured at frequencies of 1 Hz to 1 MHz in steps of factor 10. The solid symbols (●) denote data measured at 100 kHz for $NaNdFeWO_6$. (c) Temperature dependence of the real part of the permittivity around the magnetic transitions measured at 1 MHz in zero magnetic field (○) and for comparison at B = 10 T (solid lines) for $NaLaFeWO_6$ and $NaNdFeWO_6$; field and zero-field curves lie on top of each other and do not show any sharp anomalies. (d) Estimation of the effective two-point dc conductivity $\sigma'(T)$ of $NaLaFeWO_6$ as calculated from the dielectric loss $\varepsilon'' = \varepsilon_0 2\pi\nu\sigma'$ at high temperatures up to 350 K. (e) $P(E)$ hysteresis loop and (f) PUND measurement T = 5 K in zero magnetic field for $NaNdFeWO_6$.

the real and imaginary part of the permittivity for frequencies from 1 Hz to 1 MHz between 5 and 300 K. $\varepsilon'(T, \nu)$ reaches relatively high values especially for high temperatures and low frequencies. However, these data are highly dispersive. On cooling, a steplike decrease in $\varepsilon'(T, \nu)$ can be detected, which is accompanied by a peak in the dielectric loss $\varepsilon''(T, \nu)$. This smooth relaxational anomaly is strongly frequency-dependent, or in other words the frequency at which the dielectric response "freezes" (i.e., it cannot follow the electric stimulus anymore) is strongly temperature-dependent. Such highly dispersive relaxation features are not characteristic of the intrinsic polarization response of the material as expected in proper or improper ferroelectrics[41] (e.g., near a ferroelectric/multiferroic transition[42]), which would be denoted by a sharp, less dispersive anomaly. Such a sharp feature is completely absent in the dielectric data as demonstrated in Figure 10a,b. Looking at a fixed frequency of 100 kHz or 1 MHz, where the influence of residual conductivity is reduced, we find smooth $\varepsilon'(T)$ curves without any anomaly. In Figure 10c, the permittivity from the temperature regime around the magnetic transitions is displayed for a higher frequency in zero field and for 10 T, again demonstrating the absence of any anomaly and of any magnetoelectric coupling at the magnetic transitions. The idea to explain the dispersive character of the dielectric response via a relaxor ferroelectric state (intrinsic nanodomains) would need intrinsically quenched (chemical) disorder, as is present in PMN or other canonical relaxor ferroelectrics but not in the present cases. Also, it is known that relaxor ferroelectrics show a Curie(−Weiss)-like increase in the permittivity with decreasing temperature in the T regime above the relaxational step[43] as a result of the superparaelectric nature of the clusters/nanodomains. In the present case, it is the opposite: $\varepsilon'(T)$ is already decaying above the relaxational step, which is accompanied by a peak in the dielectric loss. In addition, we deal with a finite residual conductivity. Figure 10d displays the 1 Hz conductivity data of the La sample as calculated from the complex dielectric response at high temperatures up to 350 K. In this regime, the dielectric loss ε'' for low frequencies dominates the real part ε'. This type of behavior cannot be explained via a dielectric relaxation process but is due to finite conductivity, which leads to a contribution of $\varepsilon'' = 2\pi\nu\varepsilon_0\sigma'$ to the imaginary part of the permittivity. The data shown in Figure 10d can be regarded as an estimated upper limit of the two-point dc conductivity including intrinsic as well as contact and intergrain contributions. At room temperature, relatively small conductivity values have to be considered, which decrease exponentially in a semiconducting manner on the lowering of the temperature. Nevertheless, these finite values for σ define a time scale on which potential polarization currents are short cut and the ferroelectric behavior is screened. However, it also becomes clear that for high enough frequencies, ε'' is dominated by ε' (Figure 10a,b) over the whole temperature range. Thus, the absence of any sharp anomaly in the corresponding permittivity data still denotes the absence of a ferroelectric phase transition in the investigated temperature regime as outlined above.

Taking this into account together with the relaxational features and the heterogeneous, polycrystalline grain structure of the samples, everything points to the corresponding Maxwell−Wagner-type interface contributions.[44,45] The origin of the regarded dielectric response can be explained by sample inhomogeneities due to grain boundaries and electrodes together with a finite residual conductivity of the samples. At these interfaces, depletion layers are formed and lead to additional resistive and capacitive contributions analogous to Schottky diodes. These nonintrinsic contributions lead to a Maxwell−Wagner-type of relaxational response as the high interfacial capacities together with the finite resistivity of the semiconducting material form RC elements with characteristic response properties pretending to have very high permittivity values.[46] Corresponding scenarios have been observed in similar polycrystalline dielectric materials.[44,45] In the present case, two relaxational processes at temperatures above 200 K and in the regime from 20 to 200 K can be observed, which can be related to grain and electrode contributions. Most of the data displayed in Figure 10 refers to $NaLaFeWO_6$ (open symbols), but qualitatively the response of $NaNdFeWO_6$ looks the same, only shifted to slightly higher temperatures as can be seen from the comparison of the 100 kHz data in Figure 10a,b. This holds also for the magnetic field dependence of the data: the 1 MHz data (green color) is displayed in Figure 10c as measured for 0 T (open symbols) and 10 T (solid line), which, as mentioned above, does not reveal any significant field-dependent differences or magnetoelectric anomalies near the magnetic transitions in the range of 20−25 K. The intrinsic permittivity contribution can be seen only at high enough frequencies, where the nonintrinsic RC elements are short-circuited or at low enough temperatures where the intrinsic

dx.doi.org/10.1021/ic401491y | Inorg. Chem. 2013, 52, 12482−12491

semiconducting resistivity R is high enough to shift the relaxation time τ = RC to values higher than the experimental time scale given by the reciprocal stimulating frequency (Figure 10c). For $NaLaFeWO_6$, the intrinsic value for the permittivity is close to $\varepsilon' = 20$, and for $NaNdFeWO_6$, it is close to $\varepsilon' = 15$ (where, however, an experimental uncertainty of at least 10% for the determination of the absolute value has to be considered). In this low-T regime, we also performed quasi-static electric-field-driven polarization measurement as displayed in Figure 10e. The $P(E)$ curvature is almost linear and resembles the expectation for a paraelectric material with finite residual conductivity. The same result can be obtained from the PUND measurements[47] shown in Figure 10f. The sequence of two positive and two negative electric field pulses in ferroelectrics would reveal the difference between the paraelectric polarization contributions induced reversibly by the external electric field and remnant contributions from the switchable spontaneous polarization: the current response to the second positive and the second negative pulse should be smaller compared to the first pulses, respectively. This is not the case; the intrinsic dielectric response looks purely paraelectric, not ferroelectric or multiferroic. This does not contradict the polar nature of the structure, which can be interpreted as a constant background of nonswitchable electric polarization not showing up in the dynamic dielectric measurements.

However, we cannot judge a possible transition to a polar structure at higher temperatures. In the temperature range investigated up to 350 K, everything points to a structurally driven polarization. This may lead to pyroelectricity, which is difficult to measure as a result of the residual finite conductivity, but in the examined temperature and electric field range, the polarization is not switchable as demanded for ferroelectric domains and the dielectric response remains linear. Nevertheless, at elevated temperatures the effective coercive fields could decrease, and nonlinear $P(E)$ curvature might emerge. Thus, to rule out ferroelectricity one would have to measure to higher temperatures, which could lead to enhanced difficulties due to conductivity.

CONCLUSIONS

We have synthesized $NaLaFeWO_6$ and $NaNdFeWO_6$ double perovskites and determined that both compounds are monoclinic with a noncentrosymmetric $P2_1$ space group, confirmed by second harmonic generation, which is a result of the combination of the A-site layered and B-site rock salt ordering of the cations and the tilting of the octahedra. The intrinsic dielectric response of both compounds, for the investigated temperature regime up to 350 K, looks purely paraelectric, not ferroelectric or multiferroic. Electron diffraction confirms the space group and highlights a compositional nanoscale separation into Na-rich and Na-poor phases. X-ray absorption spectroscopy shows Fe^{2+} and W^{6+} formal oxidation states. The magnetic susceptibility indicates that both compounds are ordered antiferromagnetically below $T_N \approx 25$ K for $NaLaFeWO_6$ and 21 K for $NaNdFeWO_6$. The low transition temperatures are attributed to the nonlinear Fe^{2+}–O–W^{6+}–O–Fe^{2+} superexchange magnetic paths. The magnetic structure of $NaNdFeWO_6$ has been solved from neutron diffraction data with a propagation vector $k = (^1/_2\ 0\ ^1/_2)$, and both Fe and Nd have been antiferromagnetically ordered.

AUTHOR INFORMATION

Corresponding Author

*E-mail: martha@rutchem.rutgers.edu.

Notes

The authors declare no competing financial interest.

ACKNOWLEDGMENTS

This work was supported by grant NSF-DMR-0966829, Rutgers University (Board of Governor Professor Grant), and grant DOD-VV911NF-12-1-0172. Use of the Spallation Neutron Source is supported by the Division of Scientific User Facilities, Office of Basic Energy Sciences, U.S. Department of Energy, under contract DE-AC05-00OR22725 with UT-Battelle, LLC. P.S.H. and T.T.T. thank the Welch Foundation (grant E-1457) for support. C.P.G. and J.H. were supported by the German Science Foundation via SFB608. The authors acknowledge Dr. Angel Muñoz for the discussion of the magnetic structure.

REFERENCES

(1) Wang, J.; Neaton, J. B.; Zheng, V.; Nagarajan, H.; Ogale, S. B.; Liu, B.; Viehland, D.; Vaithyanathan, V.; Schlom, D. G.; Waghmare, U. V.; Spaldin, N. A.; Rabe, K. M.; Wuttig, M.; Ramesh, R. *Science* **2003**, *299*, 1719−1722.
(2) Cava, R. J.; Batlogg, B.; van Dover, R. B.; Murphy, D. W.; Sunshine, S.; Siegrist, T.; Remeika, J. P.; Rietman, E. A.; Zahurak, S.; Espinosa, G. P. *Phys. Rev. Lett.* **1987**, *58*, 1676−1679.
(3) Eerenstein, W.; Mathur, N. D.; Scott, J. F. *Nature* **2006**, *442*, 759−765.
(4) de Groot, R. A.; Mueller, F. M.; van Engen, P. G.; Buschow, K. H. J. *Phys. Rev. Lett.* **1983**, *50*, 2024−2027.
(5) von Helmolt, R.; Wecker, J.; Holzapfel, B.; Schultz, L.; Samwer, K. *Phys. Rev. Lett.* **1993**, *71*, 2331−2333.
(6) Kobayashi, K. I.; Kimura, T.; Sawada, H.; Terakura, K.; Tokura, Y. *Nature* **1998**, *395*, 677−680.
(7) Woodward, P.; Hoffman, R.-D.; Sleight, A. W. *J. Mater. Res.* **1994**, *9*, 2118−2127.
(8) Anderson, M. T.; Greenwood, K. B.; Taylor, G. A.; Poeppelmeier, K. R. *Prog. Solid State Chem.* **1993**, *22*, 197−233.
(9) Lufaso, M. W.; Woodward, P. M. *Acta Crystallogr.* **2004**, *B60*, 10−20.
(10) Anderson, M. T.; Poeppelmeier, K. R. *Chem. Mater.* **1991**, *3*, 476−482.
(11) Anderson, M. T.; Poeppelmeier, K. R.; Gramsch, S. A.; Burdett, J. K. *J. Solid State Chem.* **1993**, *102*, 164−172.
(12) Azuma, M.; Kaimori, S.; Takano, M. *Chem. Mater.* **1998**, *10*, 3124−3130.
(13) Torres-Pardo, A.; Krumeich, F.; González-Calbet, J. M.; García-González, E. *J. Am. Chem. Soc.* **2010**, *132*, 9843−9849.
(14) King, G.; Thimmaiah, S.; Dwivedi, A.; Woodward, P. M. *Chem. Mater.* **2007**, *19*, 6451−6458.
(15) Lopez, M. L.; Veiga, M. L.; Pico, C. *J. Mater. Chem.* **1994**, *4*, 547−550.
(16) Knapp, M. C.; Woodward, P. M. *J. Solid State Chem.* **2006**, *179*, 1076−1085.
(17) Fukushima, T.; Stroppa, A.; Picozzi, S.; Perez-Mato, J. M. *Phys. Chem. Chem. Phys.* **2011**, *13*, 12186−12190.
(18) Rietveld, H. M. *J. Appl. Crystallogr.* **1969**, *2*, 65−71.
(19) Rodríguez-Carvajal, J. *Physica B* **1993**, *192*, 55−69.
(20) Ok, K. M.; Chi, E. O.; Halasyamani, P. S. *Chem. Soc. Rev.* **2006**, *35*, 710−717.
(21) Kurtz, S. K.; Perry, T. T. *J. Appl. Phys.* **1968**, *39*, 3798−3813.
(22) Arillo, M. A.; Gomez, J.; Lopez, M. L.; Pico, C.; Veiga, M. L. *Solid State Ionics* **1997**, *95*, 241−248.
(23) Glazer, A. M. *Acta Crystallogr., B* **1972**, *28*, 3384−3392.

(24) Loopstra, B. O.; Boldrini, P. *Acta Crystallogr.* **1966**, *21*, 158−162.
(25) Vogt, T.; Woodward, P. M.; Hunter, B. A. *J. Solid State Chem.* **1999**, *144*, 209−215.
(26) Brese, N. E.; O'Keefe, M. *Acta Crystallogr., B* **1991**, *47*, 192−197.
(27) Guiton, B. S.; Davies, P. K. *Nat. Mater.* **2007**, *6*, 586.
(28) Garcia-Martin, S.; Urones-Garrote, E.; Knapp, M. C.; King, G.; Woodward, P. M. *J. Am. Chem. Soc.* **2008**, *130*, 15028−15037.
(29) Licurse, M. W.; Davies, P. K. *Appl. Phys. Lett.* **2010**, *97*, 123101.
(30) Garcia-Martin, S.; King, G.; Nenert, G.; Ritter, C.; Woodward, P. M. *Inorg. Chem.* **2012**, *51*, 4007−4014.
(31) Kurtz, S. K.; Perry, T. T. *J. Appl. Phys.* **1968**, *39*, 3798−3813.
(32) Popov, G.; Greenblatt, M.; Croft, M. *Phys. Rev. B* **2003**, *67*, 024406.
(33) Lin, Q.; Greenblatt, M.; Croft, M. *J. Solid State Chem.* **2005**, *178*, 1356−1366.
(34) Mandal, T.; Poltavets, V. M.; Greenblatt, M. *J. Solid State Chem.* **2008**, *181*, 2325−2331.
(35) Liang, G.; Park, K.; Li, J.; Benson, R.; Vaknin, D.; Markert, J. T.; Croft, M. *Phys. Rev. B* **2008**, *77*, 064414.
(36) Zhang, L.-L.; Liang, G.; Ignatov, A.; Croft, M.; Xiong, X.-Q.; Hung, I.-M.; Huang, Y.-H.; Hu, X.-L.; Zhang, W.-X.; Peng, Y.-L. *J. Phys. Chem. C* **2011**, *115*, 13520−13527.
(37) Kumar, Mandal, T.; Croft, M.; Hadermann, J.; Van Tendeloo, G.; Stephens, P. W.; Greenblatt, M. *J. Mater. Chem.* **2009**, *19*, 4382−4390.
(38) Li, M.-R.; Retuerto, M.; Go, Y. B.; Emge, T. J.; Croft, M.; Ramanujachary, K. V.; Dachraoui, W.; Hadermann, J.; Tang, M.-B.; Zhao, J.-T.; Greenblatt, M. *J. Solid State Chem.* **2013**, *197*, 543−549.
(39) King, G.; Wayman, L.; Woodward, P. M. *J. Solid State Chem.* **2009**, *182*, 1319−1325.
(40) Garcia-Muñoz, J. L.; Rodriguez-Carvajal, J.; Lacorre, P. *Phys. Rev. B* **1994**, *50*, 978.
(41) Ishibashi, Y.; Takagi, Y. *Jpn. J. Appl. Phys.* **1976**, *15*, 1621−1636.
(42) Kimura, T.; Goto, T.; Shintani, H.; Ishizaka, K.; Arima, T.; Tokura, Y. *Nature* **2003**, *426*, 55−59.
(43) Cross, L. E. *Ferroelectrics* **1987**, *76*, 241−267.
(44) Lunkenheimer, P.; Bobnar, V.; Pronin, A. V.; Ritus, A. I.; Volkov, A. A.; Loidl, A. *Phys. Rev. B* **2002**, *66*, 052105.
(45) Niermann, D.; Waschkowski, F.; de Groot, J.; Angst, M.; Hemberger, J. *Phys. Rev. Lett.* **2012**, *109*, 016405.
(46) Maxwell, J. C. *Treatise on Electricity and Magnetism*, 3rd ed., 1991. Wagner, R. J. *Ann. Phys. (Leipzig)* **1913**, *40*, 817.
(47) Scott, J. F. *Ferroelectric Memories*; Springer: Berlin, 2000; Chapter 6.